EES Batteries

PAPER

View Article Online
View Journal

Open Access Article. Published on 13 February 2026. Downloaded on 2/25/2026 4:41:42 AM.
This article is licensed under a Creative Commons Attribution-NonCommercial 3.0 Unported Licence.

Check for updates

Cite this: DOI: 10.1039/d6eb00019c

Design guidelines to use optical fibers as state of charge sensors: an *operando* micro wide and small angle X-ray scattering study of an IR-fiber equipped smart Na-ion battery

Yuan-Chi Yang, †[a] Yu Wang,†[b,c] Annabel Olgo,[d] Nilanka M. Keppetipola,[b,c] Zhenying Li,[b,c,e] Ozlem Sel,[b,c] Nils Blanc,[f] Benoit Mathieu,[a] Ambroise Van Roekeghem,[a] Samuel Tardif,[g] Sandrine Lyonnard,[d] Jean-Marie Tarascon*[b,c,e] and Quentin Jacquet *[d]

Received 21st January 2026,
Accepted 23rd January 2026

DOI: 10.1039/d6eb00019c

rsc.li/EESBatteries

Smart batteries are equipped with sensors that monitor temperature, state of charge, and strain during utilization. These data estimate the battery's state of health, crucial to increasing the battery life by adapting battery use and triggering self-healing mechanisms. However, few studies are devoted to the reliability of sensors. This work aims to evaluate the accuracy of state-of-sodiation determination using an optical fiber. Along that line, an optical fiber is introduced inside a Na-ion battery and used to obtain local (<1 μm around the fiber) *operando* infrared (IR) spectra of the Prussian blue analog (PBA) positive electrode material during the first three cycles. The fourth cycle is performed while the battery is scanned with a micro X-ray beam (ESRF), allowing the measurement of wide and small-angle scattering (WAXS/SAXS) maps. IR, WAXS, and SAXS are used to determine the PBA material's state of sodiation (SoS). Qualitatively, the average SoS measured by all the methods has the same trend; however, quantitatively, the SoS measured by the fiber deviates from that obtained by electrochemical and WAXS methods. We investigate the origin of this deviation with WAXS mapping. First, the SoS at the fiber position is delayed by 5–20% for the cell studied in this work. Using preliminary simulations, we qualitatively reproduce this delay when the electrode is locally compressed by the fiber. Second, the sodiation of the PBA electrode is very heterogeneous. The heterogeneity cannot be captured by a single fiber integrating the IR spectra along its surface and length. These results indicate future directions to optimize the design of smart batteries: (1) introducing the fiber without modifying the electrode, (2) using simulation to predict the compression effect and calibrate the state of sodiation determination, and (3) developing spatially resolved measurements through fiber coating or using fiber nets.

Broder context

Monitoring Li or Na-ion battery degradation during utilization is crucial to improve their lifetime by adapting the battery use conditions and to design the battery end of life (reuse or recycle). Accurate battery degradation determination requires more data, such as temperature, strain, or state-of-charge. This information can be obtained by introducing sensors inside cells or packs. Battery sensing is still a relatively new field that has grown tremendously recently. In this work, we focus on the reliability of state-of-charge sensors, particularly optical fibers capable of obtaining infrared spectra inside the battery. To achieve this goal, we employed *operando* scanning micro X-ray small and wide-angle scattering on a fiber-equipped pouch cell. This method can map with micrometer-scale resolution the battery state of charge. Comparing the infrared and X-ray scattering information, we conclude that the state-of-charge determined by the fiber and the X-ray scattering methods is qualitatively the same. However, we observed two biases for the fiber-based state-of-charge determination: (1) an electrochemical lag; (2) the presence of a heterogeneous state of charge that cannot be captured by a single fiber. Based on these observations, we propose guidelines for the design of fiber-equipped batteries.

[a]*Univ. Grenoble Alpes, CEA, Liten, DEHT, 38000 Grenoble, France*
[b]*Chimie du Solide et de l'Énergie, UMR 8260, Collège de France, Paris, France. E-mail: jean-marie.tarascon@college-de-france.fr*
[c]*Réseau sur le Stockage Électrochimique de l'Énergie (RS2E), FR CNRS 3459, France*
[d]*Univ. Grenoble Alpes, CEA, CNRS, Grenoble INP, IRIG, SyMMES, 38000 Grenoble, France. E-mail: quentin.jacquet@cea.fr*
[e]*Sorbonne Université–Campus Pierre-et-Marie-Curie, Paris, France*
[f]*Univ. Grenoble Alpes, CNRS, Grenoble INP, Institut Néel, 38000 Grenoble, France*
[g]*University Grenoble Alpes, CEA, CNRS, IRIG, MEM, 38000 Grenoble, France*
† Equal contribution.

© 2026 The Author(s). Published by the Royal Society of Chemistry

Open Access Article. Published on 13 February 2026. Downloaded on 2/25/2026 4:41:42 AM.
This article is licensed under a Creative Commons Attribution-NonCommercial 3.0 Unported Licence.

Introduction

Batteries play a key role in the electrification of society. However, there are environmental concerns about their fabrication, which is energy-intensive and heavily relies on mining. To produce fewer batteries, it is essential to increase the lifetime and promote the second life of batteries, but it requires non-destructive real-time monitoring of the state of health (SoH) to adapt battery use. SoH is a metric to evaluate the ageing level of batteries, which often includes capacity and/or power fade.[1] Moreover, in batteries equipped with self-healing strategies, SoH sensors are necessary to trigger healing procedures.[2] Consequently, SoH determination has become a priority in public and company research in recent years, as demonstrated by the importance of sensing technologies in EU funding (Battery2030+) policy, for example.[3] SoH assessment is usually performed by modelling battery degradation using either model or data-based approaches.[4] Both approaches rely on input parameters such as load curves or temperature. SoH assessment using a small number of measured parameters is poorly predictive due to the high variability of the battery use conditions and the complexity of aging mechanisms occurring at different length and time scales.[5] Adding non-destructive sensors to batteries provides extra information to parametrize these models. Optical fiber sensors are ideally suited for this purpose because of their small size, their chemical resistance in typical battery electrolytes, and the large number of parameters that can be measured by tuning the fiber properties. Indeed, strain measurements, temperature, or spectroscopic information have been successfully collected inside operating batteries.[6–10] The introduction of fibers does not affect the overall battery performance, at least over a few hundred cycles.[11,12] However, it locally delays the reaction mechanism at the fiber position, as qualitatively shown by our group using synchrotron methods to measure graphite lithiation close and far from a thermoluminescence-based optical fiber located in a prismatic Li-ion battery.[11] This delay was hypothesized to be due to the local mechanical deformation induced by introducing an approx. 200 μm fiber into an electrode stack, measuring hundreds of micrometers typically. This local effect might not be an issue for sensors measuring bulk properties such as temperature, strain, or entropy[7,13] but could cause concerns for sensors measuring the local state-of-charge (SoC) by spectroscopic methods.[14] Indeed, recent work from C. Gervilliéé-Mouravieff *et al.* demonstrated the capability to measure the SoC of $LiFePO_4$ or $Na_3V_2(PO_4)_2F_3$ from the IR spectra obtained from an optical fiber.[12] SoC sensors are critical for these materials featuring flat voltage profiles because the SoC cannot be inferred from the cell voltage value. It is therefore essential to evaluate the validity range of sensors and propose optimization strategies. This can be achieved with a multimodal approach where sensing data are compared with the SoC information retrieved independently. In this work, we use non-destructive X-ray scanning methods.

The system measured is a Na-ion pouch cell battery containing a hard carbon (HC) negative electrode and a manganese–iron Prussian blue analog (PBA) positive electrode of chemical composition $Na_{1.95}Mn[(FeCN)_6]_{0.91}\cdot 0.08H_2O$, which features a flat intercalation potential.[15] This battery chemistry is advantageous compared to typical Li-ion batteries because it is cheaper and free of critical elements such as natural graphite, Li, or Cu, while having performances close to low energy density Li-ion $LiFePO_4$-based batteries.[16] The pouch cell is equipped with a chalcogenide optical fiber embedded into the PBA positive electrode. Infrared optical fiber evanescent wave spectroscopy (IR-OFEWS) of the positive electrode during battery operation was performed, allowing the determination of the state-of-sodiation (SoS) of the active material around the fiber (<1 μm distance). The SoS is also spatially resolved in the electrode plane using *operando* micro wide and small angle scattering mapping (μWAXS and μSAXS) at the synchrotron. Using the WAXS data, we find that the SoS of the PBA positive electrode at the fiber position is delayed by up to 20% compared to its direct surroundings, confirming the lagging effect of the fiber on the local electrochemical reaction for this cell chemistry. This phenomenon is observed at low and fast C-rates, and it is very local since it completely disappears 50 μm away from the fiber. Preliminary pseudo-3D porous electrode model simulation suggests that the reason for this delay could be the reduction of the electrode porosity around the fiber position, presumably due to compression of the electrode during the introduction of the fiber. Moreover, μWAXS mapping also reveals that the biphasic sodiation of PBA occurs through a very heterogeneous reaction at the cell level. The small fiber located at the center of the cell does not capture this heterogeneity since it averages signals across the electrode length. However, reaction heterogeneity is an important parameter to understand ageing, hence highlighting the need to increase space resolution *via*, for example, specific fiber coatings.

Experimental section

Materials and methods

Materials. All the chemicals were purchased commercially and used without further purification. Sodium ferrocyanide decahydrate ($Na_4Fe(CN)_6\cdot 10H_2O$, ≥98.0%, Sigma-Aldrich), trisodium citrate dihydrate ($Na_3C_6H_5O_7\cdot 2H_2O$, 99.0%, Thermo Scientific Chemicals), sodium chloride (NaCl, 99.5%, Thermo Scientific Chemicals), and manganese(II) chloride tetrahydrate ($MnCl_2\cdot 4H_2O$, ≥99%, Sigma-Aldrich) were used for the PBA synthesis. $NaPF_6$ and propylene carbonate (PC) were purchased from Dodochem. *N*-Methyl-2-pyrrolidone (NMP) was acquired from Sigma-Aldrich. A hard Carbon (HC) electrode and powder are provided by Tiamat Company, France.

Synthesis. PBA compound was synthesized by a co-precipitation method; all details of the synthesis and characterization can be found in the work from Li *et al.*[15] Specifically, 35.9 mmol $Na_4Fe(CN)_6\cdot 10H_2O$, 142.8 mmol $Na_3C_6H_5O_7\cdot 2H_2O$, and 7.2 mol NaCl were dissolved in 1.125 L deionized water (Solution 1). Then, the co-precipitation reaction was performed

 © 2026 The Author(s). Published by the Royal Society of Chemistry

Open Access Article. Published on 13 February 2026. Downloaded on 2/25/2026 4:41:42 AM.
This article is licensed under a Creative Commons Attribution-NonCommercial 3.0 Unported Licence.

at room temperature by dropwise addition of 71.5 mmol $MnCl_2{\cdot}4H_2O$ dissolved in 500 mL deionized water (Solution 2) into Solution 1. The whole process was performed in a continuous stirred tank reactor (CSTR, Eppendorf BioFlo 320) with a stirring speed of 1000 rpm and a solution adding speed of 0.2 mL min^{-1}. Next, the resulting precipitate was collected after settling overnight and then washed several times with deionized water and ethanol. Finally, the dehydrated rhombohedral Prussian White (R-PW) was obtained by drying at 175 °C for 20 h in a vacuum (10^{-6} bar). The typical particle size is 100 nm (determined using scanning electron microscopy), while the R-PW chemical composition is $Na_{1.95}Mn[Fe(CN)_6]_{0.91}{\cdot}0.08H_2O$ as determined by inductively coupled plasma mass spectrometry (ICP) and thermogravimetric analysis (TGA). Cell parameters of the synthesized materials are a = 6.58940(10) Å and c = 18.9189(3) Å ($R\bar{3}$ space group), which is in agreement with other reports.[17]

Pouch cell fabrication. The pouch cell was fabricated following the so-called Bellcore method.[18] It consists of fabricating a flexible self-standing electrode and a separator layer laminated together to make the battery.

Positive electrode preparation. PVDF-HFP (poly(vinylidene fluoride)-*co*-hexafluoropropylene, Kynar 2801), DBP (dibutyl phthalate, Sigma Aldrich, 99%), and carbon (Super P, Alfa Aesar) were added sequentially to acetone (VWR chemicals, >99.9%), and R-PW powder was mixed and stirred overnight. The slurry was then cast on a glass plate for 5 h to complete evaporation of acetone; the tape was collected and cut into electrodes with dimensions of 3.3 × 3.8 cm. Then the film was laminated with Al mesh at 130 °C. The entire procedure was done in a glovebox. Once DBP is removed after the full cell assembly step (see below), the resulting electrode weight fraction is R-PW/PVDF-HFP/Carbon – 56/20/24 with 1.8 mAh cm^{-2} areal capacity.

Separator preparation. PVDF-HFP, DBP, and SiO_2 were added sequentially to acetone and mixed at 1200 rpm for five hours after each individual component was added. The slurry was then cast on a mylar film and left for five hours to allow complete evaporation of acetone. The tape was collected and cut into small pieces with dimensions of 4.0 × 4.5 cm.

Negative electrode preparation. PVDF-HFP, DBP, hard carbon (HC), and carbon were added sequentially to acetone and mixed at 1200 rpm for 10 min after each individual component was added. The slurry was then cast on a glass plate for five hours to complete evaporation of acetone, the tape was collected and cut into electrodes with dimensions of 3.5 × 4.0 cm. Then the HC film was laminated with Cu mesh at 130 °C and 35 psi. Once DBP is removed after the full cell assembly step, the resulting electrode weight fraction is HC/PVDF-HFP/Carbon – 86/10/4 with ~2.0 mAh cm^{-2} areal capacity.

Full cell assembly. The IR fiber ($Te_2As_3Se_5$ (TAS)) was coated with a layer of R-PW particles *via* spraying the solution of R-PW/Carbon/PVDF-HFP dissolved in acetone (weight ratio = 67/28/5). The TAS fiber was positioned between two R-PW films and laminated at 110 °C. Then the positive electrode, separator, and negative electrode were laminated together at 110 °C. The DBP was removed from the obtained cell with diethyl ether (99%, Thermo scientific), three times (15 min for each time), and the cell was then dried in a glovebox for 8 h. Finally, the cell was wetted with the electrolyte (1 M $NaPF_6$ in PC) and put into an Al packing bag with the TAS fiber fixed on the bag using epoxy and cured for 12 h. The entire procedure was done in a glovebox.

Electrochemical measurement. Up to four cells were fabricated and tested for 1st cycle *operando* IR measurement. One cell (Cell2) was measured for three consecutive cycles. Two of the best-performing cells (Cell1 and Cell2) were measured using μWAXS/SAXS mapping. The 1st cycles were performed at a C-rate of C/30 to ensure a good formation of the HC electrode (current density of 0.06 mA cm^{-2}), which corresponds to the extraction of approximately 2 Na^+ per unit formula of R-PW in 30 h. The following cycles are cycled at C/15. Cell cutoff voltages are fixed to 3.8 V and 1.5 V.

***Operando* infrared spectrum measurement.** The *operando* measurements were performed with a Fourier-transformed infrared spectrometer (T37 or Invenio S, Bruker) with an accessory connection system on the right side to focus the infrared beam on one entry extremity of the fiber. A mercury–cadmium–tellurium detector with a spectral range of 12 000 cm^{-1} to 600 cm^{-1} was used to record the optical signal at the output extremity of the fiber. During all the experiments, the mercury–cadmium–tellurium detector was cooled with liquid nitrogen. For all the experiments, the edges of the TAS fiber were cleaved manually. The signal between the input and output of the fiber was controlled, with an amplitude of around 10 000 for a 125 μm TAS fiber. IR-FOEWS spectra obtained with this method probe species at 0.5–2 μm of the fiber surface, depending on the wavelength and the medium refractive index. See calculations in the supporting information from Gervillié-Mouravieff *et al.*[12]

***Operando* SAXS/WAXS.** SAXS/WAXS mapping experiments were conducted at the BM02 beamline of the European Synchrotron Radiation Facility (ESRF), with the experimental data publicly available through the ESRF data portal (http://www.doi.org/10.15151/ESRF-ES-1058211918). The experiment utilized a beam with dimensions of 40 × 80 μm^2 and an energy of 18 keV (λ = 0.6888 Å), delivering an intensity of 1.9 × 10^{10} photons per s. The pouches were held in the beam with specially designed sample holders (Fig. S1). No pressure is applied on the electrochemical stack as the electrodes and separator are hot pressed together. The data collection employed a "horizontal fly scans" methodology, enabling fast X-ray scanning of the cell. In each so-called "Bigmap" scan, the pouch cell moved continuously horizontally along the x-axis from 0 to 31 mm with the shutter remaining open. During this movement, detector images were averaged over each 1 mm increment. After completing each horizontal scan, the sample was shifted 1 mm vertically before initiating the next horizontal scan, producing comprehensive 2D maps. The mapping covered the entire electrode surface, generating 30 × 31 pixel maps with a 1 mm × 80 μm pixel size. After each

Open Access Article. Published on 13 February 2026. Downloaded on 2/25/2026 4:41:42 AM.
This article is licensed under a Creative Commons Attribution-NonCommercial 3.0 Unported Licence.

Bigmap scan, a more resolved "Smallmap" scan was also performed (the areas highlighted with blue frames as shown in Fig. 4a) to visualize the vicinity around the optical fiber. In each Smallmap, five horizontal fly scans with 3.5 mm vertical spacing were performed, generating 150 × 5 pixel maps with a pixel size of 40 μm × 80 μm. One Bigmap–Smallmaps cycle takes approximately 14 minutes. SAXS and WAXS patterns were collected simultaneously for each pixel using two different detectors: an imXPAD WOS detector for WAXS positioned 11.6 mm behind the sample and having a hole in its center and an imXPAD S540 detector for SAXS located 3544 mm behind the sample and used to collect the scattered beam that passed through the first detector hole. Calibration of the sample-to-detector distances was performed using reference materials, specifically silver behenate ($AgC_{22}H_{43}O_2$) for SAXS and lanthanum hexaboride (LaB_6) for WAXS. Dose calculations, based on the work of T. Jousseaume *et al.*,[19] demonstrated that the radiation exposure reached 85 kGy for the positive electrode and 2 kGy for the negative electrode, both remaining below the estimated damage threshold.[19,20]

Data analysis

Integration correction and background removal. Azimuthal integration was performed with PyFAI,[21] normalizing patterns by the incoming (I_o) and transmitted (I_t) photon flux. While data acquisition was continuous during electrochemical cycling, WAXS patterns underwent pixel-by-pixel recalibration using the Cu peak position to correct for position differences between the LaB_6 reference and electrode by using the formulas below in which Q_{obs}, Q_{th} and λ are the observed peak position before calibration, its theoretical value and the wavelength:

$$Q_{new} = \frac{4\pi}{\lambda} \sin\left(\frac{1}{2}\tan^{-1}\left(\frac{1}{K\tan\left(2\sin^{-1}\left(\frac{\lambda q\pi}{4}\right)\right)}\right)\right)$$

where K is defined by:

$$K = \frac{\tan\left(2\sin^{-1}\left(\frac{\lambda Q_{obs}\pi}{4}\right)\right)}{\tan\left(2\sin^{-1}\left(\frac{\lambda Q_{th}\pi}{4}\right)\right)}$$

Minimal Cu peak position changes during electrochemical cycling confirmed negligible pouch movement (Cu peak position is $3.47 \pm 6 \times 10^{-3}$ Å), eliminating the need for time-dependent Q-range calibration. Background subtraction was performed using Prisma[22] software's symmetric Least-Squares smoothing method (AsLS).

SAXS/WAXS and IR data analysis. To estimate the Na concentration in the PBA positive electrode from *operando* WAXS data, three peaks between 1.15–1.32 $Å^{-1}$ were considered. They correspond to two Bragg reflections from desodiated tetragonal Prussian Yellow (T-PY) (002), (200), and one reflection from sodiated rhombohedral Prussian White (R-PW) (012). Peaks were fitted with Gaussian functions to extract peak areas and positions. Regarding the *operando* IR spectrum, the cyanide group vibrations of R-PW and T-PY are located at 2055 cm^{-1} and 2178 cm^{-1}, respectively. Their area was extracted by integrating peak intensities between 2025–2100 cm^{-1} and 2150–2200 cm^{-1}.

The Na concentration and the state of sodiation (SoS) are not directly proportional to the IR and WAXS peak intensity ratios. Indeed, R-PW and T-PY phases exhibit different scattering efficiencies in WAXS and different absorbance strengths in IR spectroscopy. Therefore, a correction factor must be applied. Assuming the system undergoes a purely biphasic transformation, in which all disappearing R-PY is fully converted into T-PY, the correction factor k is determined using the following equation:

$$k = \frac{\left|\frac{dA_R}{dt}\right|}{\left|\frac{dA_T}{dt}\right|}$$

k_{WAXS} = 0.641 and k_{IR} = 2.057 and the peak area fraction of R-PW is computed by the equation:

$$\text{Peak area fraction of R-PW} = \frac{A_R}{A_T k + A_R}$$

The SoS for the hard carbon negative electrode was approximated by integrating the area under the 1D SAXS profile in the Q-range [0.08–0.3 $Å^{-1}$] (corresponding to nanopores smaller than 10 nm). A higher normalized value indicates a lower SoS of the hard carbon electrode. The SoS of the $Na_{1.95}Mn[(FeCN)_6]_{0.91}\cdot 0.08H_2O$ (MnFePBA) positive electrode was approximated similarly by integrating the area in the low Q-range [0.005–0.02] $Å^{-1}$, which corresponds to the size of MnFePBA particles, approximately 100 nm in diameter.

P3D simulation details

Electrolyte properties. The bulk electrolyte diffusivity is taken as:

$$D = 7 \times 10^{-10}\ \text{m}^2\ \text{s}^{-1}$$

In the separator, the effective diffusivity is:

$$D_{sep} = D \cdot \varepsilon^{1.5}, \quad \varepsilon_{sep} = 0.3,$$

where ε is the porosity. While in the electrodes, it is expressed as:

$$D_{elec} = \frac{D \cdot \varepsilon}{\tau}, \quad \tau_{elec} = 3$$

where τ is the tortuosity, a sensitive parameter. A relatively low value is chosen for the system.

The ionic conductivity of the electrolyte is concentration-dependent and follows the Ecker correlation:

$$\kappa(c) = 0.4 \times (1.726 + 17.919c - 12.983c^2 + 2.667c^3)$$

where c is the ion concentration in the electrolyte (mol l^{-1}). The nominal value is c_0 = 1, but it evolves locally during cycling. The effective conductivity for the separator is given by:

 © 2026 The Author(s). Published by the Royal Society of Chemistry

Open Access Article. Published on 13 February 2026. Downloaded on 2/25/2026 4:41:42 AM.
This article is licensed under a Creative Commons Attribution-NonCommercial 3.0 Unported Licence.

$$\kappa_{\text{sep}} = \frac{\kappa}{6}$$

And for the electrodes:

$$\kappa_{\text{elec}} = \frac{\kappa \cdot \varepsilon}{\tau}$$

Electrode structure. The simulated system consists of a hard carbon (HC) negative electrode with a thickness of 120 μm, a separator of 50 μm, and a Prussian blue analog (PBA) positive electrode of 250 μm. An optical fiber is modeled as an inactive semi-cylindrical region with a diameter of 125 μm. The Prussian Blue Analogue (PBA) for the first configuration has a uniform porosity of ε = 50%. In the second configuration, the porosity of the electrode varies as a function of the position along the *x*-axis, as shown in Fig. 6a. In contrast, the hard carbon (HC) electrode has a porosity of ε = 0.2 for both configurations. The electronic conductivity of the active material is not considered the limiting factor in this study.

Active material property. The solid-state diffusion coefficients of the active materials are set to $D_{\text{PBA}} = 5 \times 10^{-13}$ m^2 s^{-1} and $D_{\text{HC}} = 5 \times 10^{-13}$ m^2 s^{-1}. The reference exchange current densities are taken as $i_{0,\text{PBA}} = 2$ A m^{-2} and $i_{0,\text{HC}} = 2$ A m^{-2}. Assuming spherical geometry, the average particle diameters are $d_{\text{PBA}} = 10$ μm and $d_{\text{HC}} = 8$ μm for HC. The open-circuit voltages (OCV) for both electrodes are measured from half-cell electrochemical data.

Electrochemical parameters. The applied current density is 2.3 mA cm^{-2}, corresponding to a C/2 rate. At the beginning of the simulation, the PBA positive electrode is uniformly sodiated to a state of 0.6, while the HC negative electrode is at a state of 0. The cell is cycled between positive electrode sodiation states of 0.1 and 0.7, with charge and discharge termination controlled by time.

Results and discussion

Cell fabrication and electrochemical performance

Rhombohedral Prussian White (R-PW) synthesis and dehydration steps are described by Li *et al.*[15] Using this material, four fiber-equipped pouch cells are built based on the Bellcore method[18] (Fig. 1a–c). First, the TAS optical fiber is embedded inside a carbon/polymer/R-PW matrix through spray-coating with a formulated ink. After drying, this results in a micron-sized thick coating at the fiber's surface as observed by scanning electron microscopy (SEM) (Fig. 1c). The fiber is then hot pressed between two 3.5 × 4 cm self-standing electrodes of R-PW, resulting in a 250 μm thick electrode. Finally, the pouch cells are assembled by laminating the fiber-equipped positive electrode with a separator made of PVDF-HFP and a hard carbon negative electrode, as observed in the SEM image of the pouch cell cross-section (Fig. 1b). Note that all the fabrication steps are performed in an Ar-filled glovebox to prevent water exposure of R-PW. The formation cycle was performed while obtaining the *operando* IR spectra. The two cells having the highest capacity and coulombic efficiency were selected for further IR and X-ray scattering measurements. In the following, we show the best cells (Cell1 and Cell2) results.

The fiber-equipped pouch cell is cycled at C/30 and C/15 (corresponding to 0.06 and 0.12 mA cm^2) for the 1st and subsequent cycles, respectively, in the voltage range of 1.5–3.8 V, with the corresponding electrochemical curve shown in Fig. 1d. The first charge features a sloppy profile corresponding to 70 mAh $g_{\text{R-PW}}^{-1}$ followed by a plateau at 3.5 V up to 155 mAh $g_{\text{R-PW}}^{-1}$. $Na_{1.95}Mn[(FeCN)_6]_{0.91}\cdot 0.08H_2O$ desodiation occurs through a single voltage plateau,[15,17] hence the shape of the voltage curve corresponds to the reaction occurring at the HC electrode. Indeed, the HC electrochemical curve comprises a slope and a plateau region.[23] After the first charge, and based on the specific capacity, 1.6 Na^+ are extracted from PBA. The subsequent discharge capacity is 108 mAh g^{-1}, corresponding to a coulombic efficiency of 70%. The 1st cycle coulombic efficiency is attributed to the solid-electrolyte interphase (SEI) formation on the negative electrode side.[23] The subsequent cycles feature sloppy and flat voltage profiles with a coulombic efficiency of 95% and a specific capacity around 90 mAh g^{-1} (corresponding to 1 Na^+ (de)sodiation from PBA). Our cell performance is representative of the R-PW//HC chemistry since recent reports for 18 650 cells showed a capacity of 120 mAh g^{-1} at the first discharge with 80% coulombic efficiency.[15] However, our cell has a lower coulombic efficiency during cycling, and hence stronger ageing, presumably due to the less optimized/homemade electrode and cell assembly using Bellcore technology. However, this is not an issue since we only study the reaction mechanism and heterogeneity over the first four cycles.

Principle of combined *operando* IR and SAXS/WAXS

The first cycle of Cell1 is performed while performing *operando* IR spectroscopy (Fig. 1f), and the fourth cycle is performed during the *operando* μSAXS/WAXS mapping (Fig. 1g). The principle of IR *operando* measurement inside 18 650 cells can be found in the work of Gervillié-Mouravieff *et al.*[12] The same methodology was implemented here into pouch cells. In short, the obtained IR spectra originate from the very surface (<1 μm) of the optical fiber inside the pouch and are averaged across the length of the fiber (approx. 4 cm). IR spectra obtained in the pouch for the pristine and charged PBA feature only two peaks in the 2000–2200 cm^{-1} wavenumber range, which are attributed to the C≡N vibration modes in sodiated (2055 cm^{-1}) and desodiated PBA (2178 cm^{-1}).[15] These peaks are very clearly observed, showing the possibility to monitor the SoS.

In the *operando* μSAXS/WAXS mapping experiment, the pouch is held in front of a microfocused X-ray beam of 40 × 80 μm^2 in the vertical and horizontal directions, respectively. The fiber direction is vertical. The X-ray beam is scattered by the cell components and the scattered beam is measured after the pouch cell by two detectors placed one after the other along the beam direction, to collect WAXS and SAXS data, respectively (Fig. 1g). The WAXS data allow us to examine crystalline structures and in particular the phase fraction between the Na-rich R-PW and the Na-poor T-PY using the relative

Open Access Article. Published on 13 February 2026. Downloaded on 2/25/2026 4:41:42 AM.
This article is licensed under a Creative Commons Attribution-NonCommercial 3.0 Unported Licence.

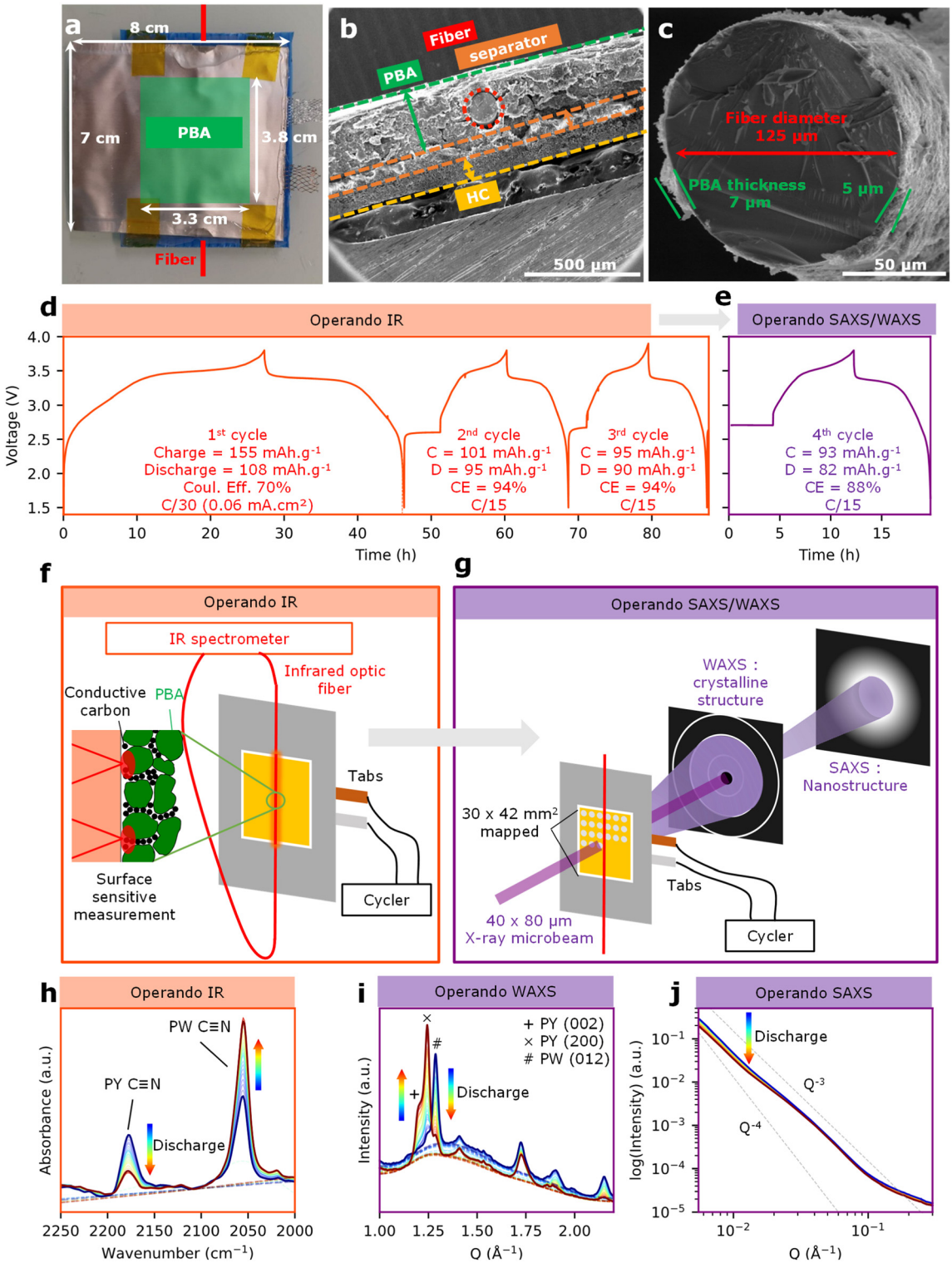

Fig. 1 (a) The picture of the fiber pouch cell with dimensions of 7 × 8 cm. (b) and (c) are images of the SEM cross-section of the fiber pouch cell and the PBA-coated optical fiber, respectively. (d) and (e) Voltage (V) *vs.* time (h) profile of the cell 1 for the first three cycles (*operando* IR measurement performed during the 1st cycle) in orange and the 4th cycle (*operando* SAXS/WAXS) in purple, respectively. (f) and (g) Illustration of the experimental setup of both measurements, respectively. The colors of the frame and voltage profiles highlight the *operando* technique applied to the cell while cycling (orange for IR, purple for SAXS/WAXS). (h), (i), and (j) The acquired raw data from *operando* IR, WAXS and SAXS, respectively. In (j) the obtained SAXS profiles show a decaying intensity comprised between a Q^{-4} and Q^{-3} power law typical of sharp-to-rough particle interfaces.

 © 2026 The Author(s). Published by the Royal Society of Chemistry

Open Access Article. Published on 13 February 2026. Downloaded on 2/25/2026 4:41:42 AM.
This article is licensed under a Creative Commons Attribution-NonCommercial 3.0 Unported Licence.

intensity of the $(012)_{\text{R-PW}}$ and $(200)_{\text{T-PY}}$ (Fig. 1i). The averaged SAXS patterns are shown in Fig. 1j and feature a decaying intensity as the scattering vector Q increases. The signal is unshaped but shows some intensity modulations departing from a pure power law behavior (*e.g.* Porod regime, $Q^{-\alpha}$ with $3 < \alpha < 4$), indicating contributions from both rough interfaces and nanoscale characteristic features. By comparing the scattering intensities of all the separated individual pouch cell components (Fig. S3), R-PW is found to dominate the signal at small Q values in the Porod regime (0.0055–0.02 Å^{-1}), while the HC signal is producing an excess intensity at higher Q values (0.08 to 0.3 Å^{-1}). The R-PW SAXS signal originates from the particle surface contribution as described by the Porod theory, while the HC intensity at high Q is due to the presence of nanosized porosity in this material, as reported in other studies.[24] Note that the surface contribution from hard carbon particles is also detected in the low Q region, but can be neglected because HC particles are much bigger (a few microns) than PBA (100 nm typically). Hence, their specific surface is much smaller, reducing the scaling factor of the $Q^{-\alpha}$ low-Q contribution by an order of magnitude with respect to PBA.

Qualitative state of charge analysis probed by *operando* IR, WAXS and SAXS. Before spatially resolving the (de)sodiation mechanism, spatially averaged WAXS and SAXS pattern evolution during cycling is analyzed and compared with the *operando* IR measurement. Regarding the IR spectra during the charging (desodiation of PBA), the peaks at 2055 cm^{-1} and 2178 cm^{-1}, corresponding to R-PW and T-PY, respectively, do not demonstrate a shift in the position but exhibit a continuous change in intensity; namely, the intensity of the R-PW peak decreases while the T-PY peak increases (Fig. 2a). This behavior is observed over the first three cycles of Cell2 and the 1st cycle of Cell1 (Fig. S5), confirming that PBA undergoes a biphasic transition from R-PW to T-PY during desodiation.[15] Regarding the relative peak intensity, before the formation cycle, only the R-PW peak at 2055 cm^{-1} is observed. At the end of the charge, R-PW is still visible along with the T-PY peak, indicating an incomplete reaction. After the formation cycle, the T-PY peak does not disappear, showing that the reaction is not fully reversible, in agreement with the cell-level coulombic efficiency. The concomitant presence of both R-PW and T-PY peaks is observed during the following cycles. The biphasic nature of the PBA electrode is further confirmed with WAXS data. Indeed, the intensities of the $(002)_{\text{T-PY}}$ and $(200)_{\text{T-PY}}$ Bragg peaks increase linearly during the desodiation of the PBA electrode. In contrast, the intensity of the $(012)_{\text{R-PW}}$ Bragg peak decreases (Fig. 2b). At the end of the desodiation of the PBA electrode, it is observed that both R-PW and T-PY Bragg peaks are present in the WAXS profile, meaning that the electrode is never fully desodiated during the charging process, which is in agreement with the IR data. Finally, the collected SAXS profiles obtained during electrochemical cycling demonstrated changes in intensities in both low and high Q regions. First, during the charging process, the scattering intensity decreased in both areas (Fig. 2c), indicating changes in the electronic density contrast due to compositional variations at the probed length scales, and/or decreasing specific surface area in the low Q region; the decrease in intensity can be attributed to the decrease of the PBA electronic density due to the volume expansion and desodiation during the R-PW to T-PY phase transition. The SAXS intensity evolution in the high Q range is consistent with a decrease in contrast between the carbon matrix and nanopores due to the pore-filling mechanism.[24] Overall, there is good qualitative agreement between the evolution of the IR and WAXS data. Both techniques show the presence of a biphasic reaction and an incomplete (de)sodiation of the PBA electrode, which is consistent with the SAXS data. However, this rough comparison needs to be further evaluated. The R-PW peak fraction (Fig. 3a and b) is calculated from (1) the electrode-averaged WAXS and (2) the IR from the fiber (see Methods). The peak fraction obtained from WAXS evolves linearly with capacity as expected from the galvanostatic cycling conditions. However, it is not the case of the SoS obtained from IR, which deviates notably from linearity at the end of charge and discharge. Clearly, the optical fiber is not precisely measuring the cell-level SoS. In the next section, we use the spatially resolved WAXS and SAXS patterns to investigate the origin of this deviation.

Spatially resolving state of charge

During the *operando* SAXS/WAXS experiment, the pouch is continuously scanned in the vertical and horizontal directions, producing 2D maps in which each pixel contains both WAXS and SAXS data. Two types of mapping measurements were performed, as shown in Fig. 4a and b: (1) entire electrode map (30 mm vertical × 42 mm horizontal) with a pixel size of 1 mm × 80 μm to obtain information on the cell level (called hereafter "Bigmap") and (2) fiber zooms consisting of five horizontal lines across the optical fiber at different vertical positions in the cell with a pixel size of 40 μm × 80 μm (called hereafter "Smallmap"). The SoS of PBA and HC electrodes is obtained for each position in the cell using (1) the WAXS peak area fraction for PBA and (2) integrated SAXS intensities for HC. First, we focus on the PBA "Bigmaps" (Fig. 4c). At the beginning of the charge, the Na-rich R-PW phase is predominant (red color, Fig. 4c); however, there is a substantial in-plane heterogeneity with some regions featuring only 20% of R-PW appearing in blue on the map. During desodiation, the R-PW transforms into the T-PY; hence, the general peak fraction of R-PW decreases (the color in Fig. 4c progressively changes from red to blue). At the end of the charge, the R-PW peak fraction is inferior to 20% in most of the pouch. During sodiation, some regions appear to sodiate more than others, which leads to a substantial heterogeneity of R-PW peak fraction at the end of discharge. Although the Na-rich regions are mostly located at the center of the pouch, the R-PW phase distribution is not exactly similar between the beginning and the end of the cycle. Furthermore, regarding the Bigmaps representing high Q region (HC region) SAXS integrated intensities across the pouch cell, it appears that the HC electrode also demonstrates SoS heterogeneities (Fig. 4d). Moreover, on the Bigmaps collected at 3.36 V during discharging, the spatial distribution of

Open Access Article. Published on 13 February 2026. Downloaded on 2/25/2026 4:41:42 AM.
This article is licensed under a Creative Commons Attribution-NonCommercial 3.0 Unported Licence.

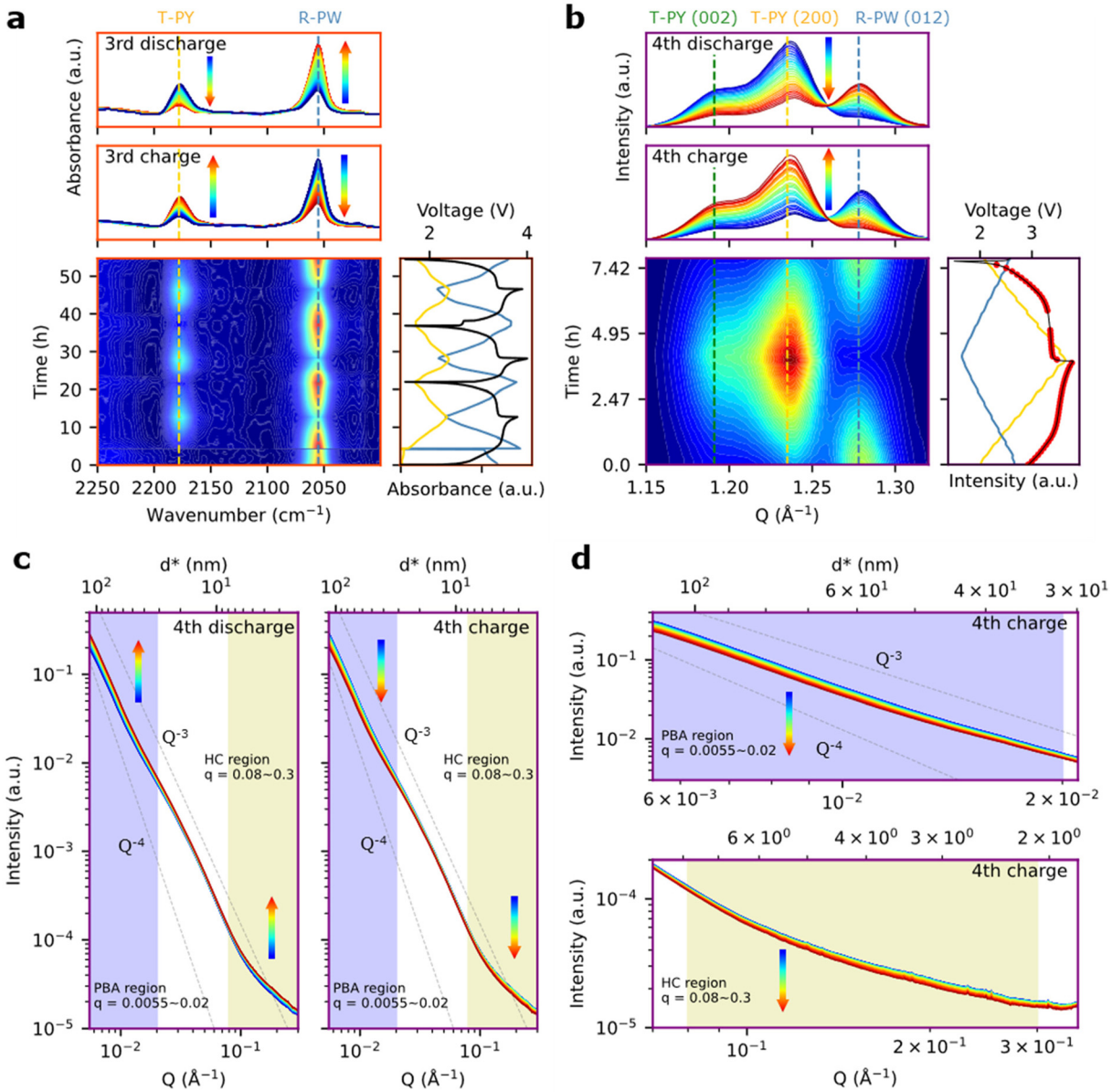

Fig. 2 (a) *Operando* IR contour of the first three C/15 cycles of Cell 2. The colors on the map represent the intensity from low to high in blue to red, respectively. The data of Cell 1 are shown in Fig. S5. The IR spectra obtained during the 3rd charge and discharge are presented on top. The colors of the arrows indicate the spectrum evolution. The IR peak intensities of R-PW (blue) and T-PY (yellow) and the voltage profile are presented on the right. (b) Spatially-averaged *operando* WAXS contour of the 4th C/15 cycle of Cell1. The data are presented as in (a). (c) Spatially-averaged *operando* SAXS of the 4th C/15 cycle. The blue and yellow shaded areas highlight the *Q* range where the intensity variation is mainly contributed by PBA and HC, respectively. (d) zoom of panel (c) in the PBA and HC regions on the top and bottom, respectively.

the HC electrode SoS heterogeneities matches the SoS heterogeneities quantified on the PBA electrode, suggesting that the local electrodes' SoS might be correlated. In conclusion, the Bigmaps reveal that both PBA and HC electrodes exhibit SoS heterogeneities at the cell level during charging and discharging.

In order to gain insight into SoS heterogeneities with a better resolution and around the 150 μm diameter fiber during electrochemical cycling, we collected so-called "Smallmaps" having a horizontal resolution of 40 μm. Focusing on the R-PW peak fraction before the charge, we observe that the four different horizontal lines scanned at different vertical positions across the fiber show different SoS heterogeneity profiles. The top line peak fraction changes from 95% to 40% going from left to right (5 mm distance), with an abrupt change spanning over 250 μm between the Na-rich and Na-poor domains (Fig. 4d). The second line is only scanning a Na-rich domain. The third and fourth lines show the presence of narrow domains <100 μm of Na-poor and Na-rich phases. These results show that SoS heterogeneity occurs

 © 2026 The Author(s). Published by the Royal Society of Chemistry

Open Access Article. Published on 13 February 2026. Downloaded on 2/25/2026 4:41:42 AM.
This article is licensed under a Creative Commons Attribution-NonCommercial 3.0 Unported Licence.

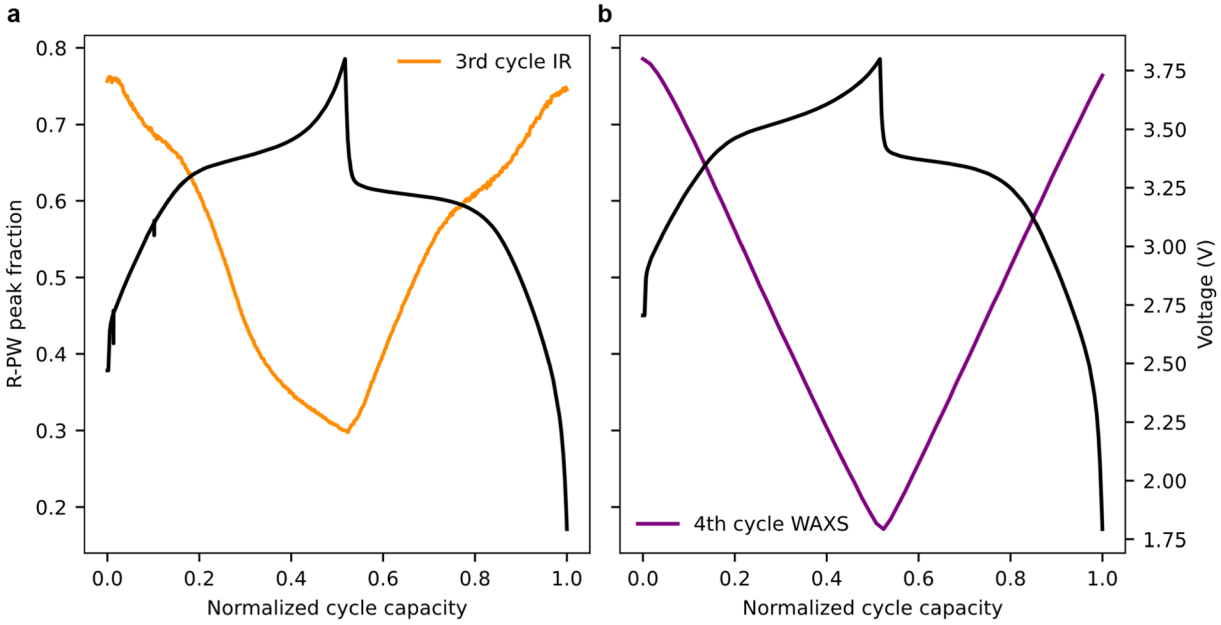

Fig. 3 (a) and (b) are showing the SoS obtained from the IR data (3rd cycle – Cell2) and the cell-averaged WAXS data (4th cycle – cell1) respectively. The black curve shows the voltage profiles.

at different length scales from 100 μm to several mm^2. These heterogeneities are important to describe the reaction mechanism at the cell level, and especially the ageing, which has been shown to induce stronger heterogeneity.[25–27] However, such inhomogeneity cannot be spotted by a single IR fiber without spatial resolution. This will be discussed in more detail in the following section.

Turning to the evolution of the Smallmaps during charge and discharge, interestingly, the maps demonstrate a vertical line spanning across the scanning lines (dotted rectangle in Fig. 4d), corresponding to the fiber position in the cell. Indeed, at the position of the fiber, the R-PW peak fraction values are always higher than those of its surroundings, indicating a higher SoS and delayed PBA reaction mechanism at the fiber position. The minimum and maximum delays during the cycle, which are obtained from the difference between the average WAXS SoS at the fiber position and the cell average WAXS SoS, are 5% ± 5% and 20% ± 10%, respectively (Fig. 4e). The delay for cell2 has the same order of magnitude (Fig. S9). The large errorbars, calculated from the SoS delay over four different positions in the cell, suggest that the delay is very sensitive to the electrode parameters. A sensitivity analysis of the delay with respect to electrode morphology should be carried out to predict the delay values for different electrodes. Moreover, the electrochemical lag is found really just at the fiber position since the SoS determination 40 μm away is already matching the overall SoS of the Smallmaps (Fig. S7). The delay of the HC electrode at the fiber position is unfortunately difficult to estimate because the strong SAXS signal originating from the fiber is masking the HC signal (Fig. S8). The delay of the electrode reaction at the fiber position was demonstrated by Olgo *et al.* on prismatic Li-ion cells.[11] Our findings complete this previous work by quantifying the delay and showing that it does not extend out of the fiber position.

Overall, thanks to the spatial resolution of the *operando* WAXS/SAXS experiment, we raise two questions on how to improve battery SoS determination using an optical fiber: (1) How can we capture reaction heterogeneity using fibers? (2) What is the origin of the electrochemical delay, and how to take it into account?

Discussion

Our experimental results demonstrate that IR-OFEWS using an optical fiber can qualitatively capture the SoS of the PBA electrode, but that it is not yet quantitative due to two main mechanisms: (1) (de)sodiation of PBA is heterogeneous on a scale of millimeters to 100 μm, and this heterogeneity cannot be captured by a single fiber without spatial resolution; (2) the electrochemical reactions at the fiber position are disrupted, resulting in higher SoS values compared to the surrounding regions. In the following, we discuss strategies to lift these challenges.

Mapping reaction heterogeneity with fibers

For the first point on the heterogeneity, a thought experiment is conducted to investigate the positional dependency of the SoS measurement. This "experiment" involved the hypothetical placement of multiple virtual optical fibers across the pouch cell, each probing the SoS without perturbing the electrochemical reactions. These virtual fibers were simulated by combining the WAXS data from a column of pixels in the Bigmap, with each fiber covering a 1.5 mm^2 surface area,

Open Access Article. Published on 13 February 2026. Downloaded on 2/25/2026 4:41:42 AM.
This article is licensed under a Creative Commons Attribution-NonCommercial 3.0 Unported Licence.

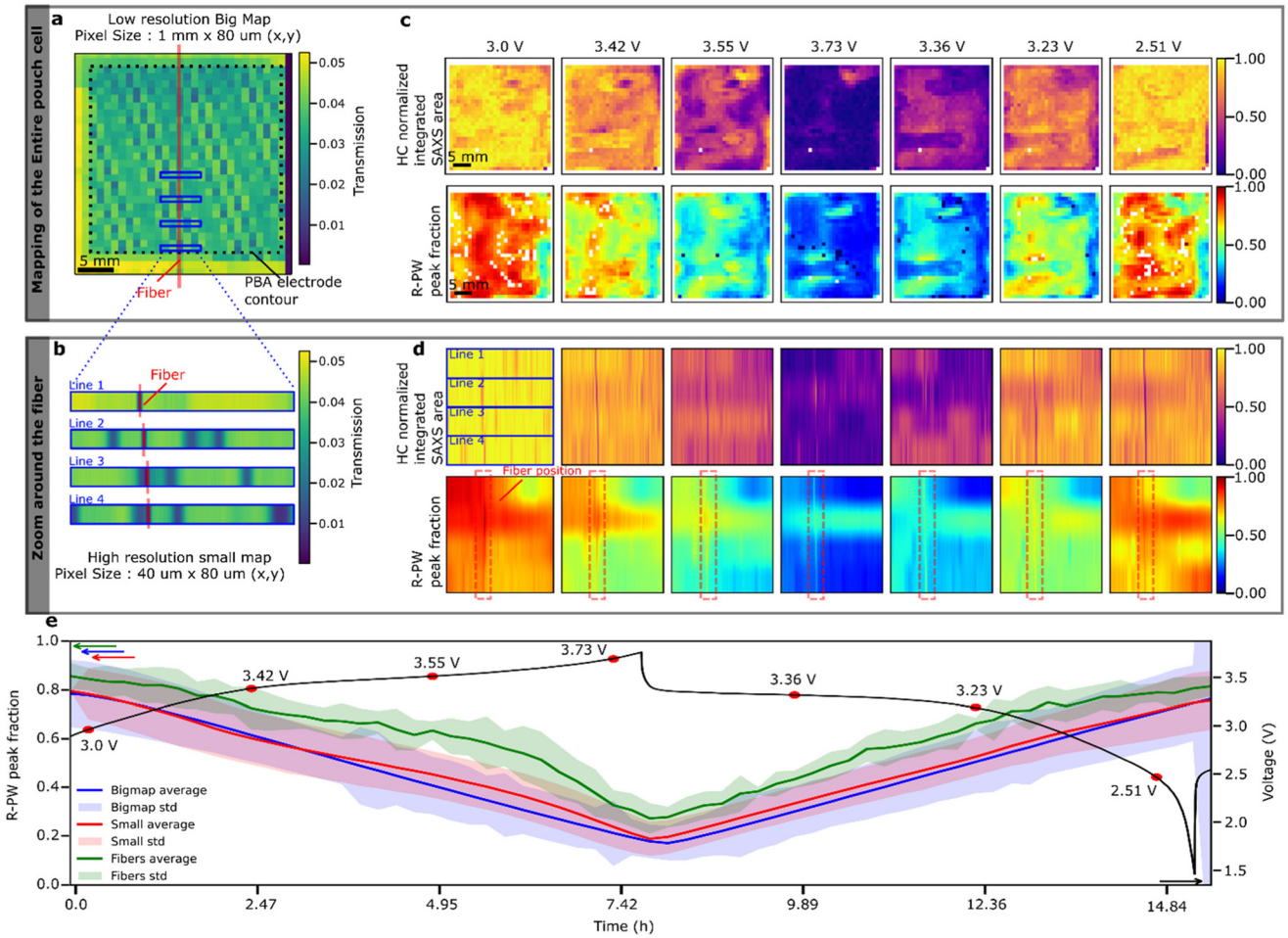

Fig. 4 (a) Transmission map of the pouch cell. The dotted frame indicates the electrode position, while the red line marks the optical fiber. The periodic mosaic pattern in the transmission stems from the Al and Cu current collector meshes. The four solid blue frames correspond to the scanned regions of the small maps shown in (b). (c) Full-electrode mapping (Bigmap) using SAXS (top) and WAXS (bottom). (d) Focused mapping in the vicinity of the optical fiber (Smallmaps), in which the red dotted frames mark the position of the optical fiber. Two sets of color maps distinguish the SAXS data from the hard carbon negative electrode and the WAXS data from the PBA positive electrode, which are used to extract the SoS from structural information. (e) The voltage profile of the 4th cycle, with red dots marking the voltages at which maps were recorded. Additionally, it shows the average SoS (solid lines) and the SoS distribution (shaded areas) for each region. Similar data analysis is available for Cell 2 (Fig. S9).

larger than the actual fiber's 0.37 mm^2 sensing area but comparable in scale. A total of 28 virtual fibers were modeled. The results revealed significant variations in SoS measurements among the virtual fibers (Fig. 5). Fibers located in sodium-rich regions consistently overestimated the SoS, whereas those in sodium-deficient regions underestimated it. This finding demonstrates that SoS measurements are highly dependent on the fiber's position within this electrode.

What about other cells and chemistry, are reactions heterogeneous in batteries? Thermodynamically, in all biphasic materials, *i.e.* featuring a flat electrochemical profile such as $LiFePO_4$, graphite or $LiMn_2O_4$, Li(Na)-poor and Li(Na)-rich phases coexist hence leading to an intrinsically heterogeneous system. The length scale at which this heterogeneity appears (particle, electrode, cell level) is not yet completely understood in the literature since it depends on many factors such as the electronic/ionic conductivities, pressure, and electrode balancing.[28,29] From our results, in this system, the heterogeneity is present at the cell level. There are no other reports of the reaction heterogeneity in PBA or HC; however, electrode level heterogeneity has been observed in other cell or chemistries. Our team observed in plane heterogeneity in the $LiNiO_2$/graphite single layer Li-ion pouch cell due to the presence of an oversized anode or in graphite/Si composites.[30,31] Other teams observed heterogeneities in Li-ion 18 650 cylindrical cells[26,32,33] showing that cell level heterogeneity is a common characteristic of alkali-ion batteries. However, heterogeneities depend on multiple parameters; therefore, the heterogeneity values reported cannot be applied directly to other chemistries or cell formats.[34]

This outcome highlights the need for fibers capable of giving 2D SoC information. There are different approaches to reach this goal: (1) using a net of TAS fibers mapping the cell-level reaction mechanism in 2D; (2) using distributed optical

 © 2026 The Author(s). Published by the Royal Society of Chemistry

Open Access Article. Published on 13 February 2026. Downloaded on 2/25/2026 4:41:42 AM.
This article is licensed under a Creative Commons Attribution-NonCommercial 3.0 Unported Licence.

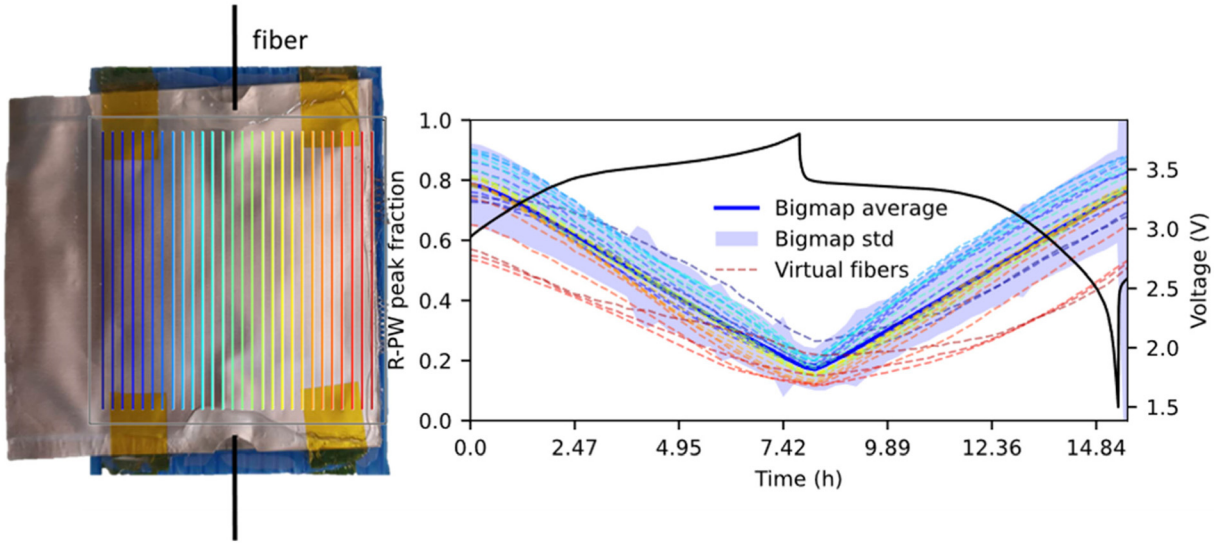

Fig. 5 The left figure illustrates how the virtual fibers are placed in the pouch cell. The right figure shows the voltage profile and the R-PW average SoS (solid lines), the SoS distribution (shaded areas), and the SoS measured by each virtual fiber (dashed lines). The color of each fiber on the left matches that of the SoS profile of each virtual fiber.

fiber sensing technology. For the first point, there are no reports to the best of our knowledge using this approach, which is practically difficult to implement due to the fragile nature of TAS fiber and the need to obtain multiple IR spectra at the same time. For the second point, there are optical fibers capable of spatially resolving temperature/strain along their length using Rayleigh light scattering. Huang *et al.* successfully implemented this strategy to measure temperature gradient with a single fiber inside a Na-ion 18 650 cell cycled at different speeds of charge.[35] Li *et al.* used a similar approach to measure strain in a $LiFePO_4$/graphite pouch cell and proposed a data analysis approach to convert strain into SoC.[36] Moreover, by winding the fiber in the pouch cell, 2D SoC mapping of the pouch cell could be performed. Spatially resolving physical parameters with fibers still has challenges to tackle: (1) the spatial resolution is limited to >1 mm (unless the signal/noise ratio can be improved[35]); (2) conversion of strain into SoC requires careful calibration because the strain/SoC relationship depends on ageing in a non-linear way. Therefore, the development of SoC monitoring by optical fibers needs to be performed hand in hand with other non-destructive characterisation techniques providing reference data on selected cells or cycling conditions. Synchrotron methods are capable of measuring the SoC at different length scales in custom or commercial cells and hence are ideally suited for this task.

Why are the electrochemical reactions at the fiber position always perturbed?

In this work, we quantified the fiber-induced electrochemical delay in a PBA positive electrode within a Na-ion single-layer pouch cell, finding a delay of 5(±5)–20(±10)%. The origin of this effect remains unclear due to the limited number of reports. Nevertheless, the ability to predict fiber-induced electrochemical lag would be highly valuable for correcting such artifacts.

To investigate the impact of embedding a fiber within an electrode on SoC heterogeneity, we performed preliminary calculations using a pseudo-3D (P3D) porous electrode Newman-type model. The optical fiber was modeled as an inactive material in this model (Fig. 6a and b). Note that some of the simulation parameters are still unknown or under debate for PBA (diffusion coefficient, charge transfer coefficient). Moreover, we have not performed a detailed quantification of the electrode microstructure (porosity, tortuosity). Therefore, our simulation results are not expected to yield quantitative information and will be used qualitatively to test two lag origin hypotheses. In the first (model 1), a hole was introduced at the center of the PBA electrode, thereby reducing the amount of active material at the fiber location while maintaining uniform porosity and tortuosity throughout the electrode. In the second (model 2), porosity around the fiber was reduced to preserve uniform in-plane PBA mass, assuming that the fiber compresses the surrounding material and thereby locally increases tortuosity. Note that model 2 is probably closer to our experimental system, since the fiber was hot pressed between two electrodes. Both configurations were simulated at a current density of 2.3 mA cm^{-2} (C/2) for two charge–discharge cycles.

With both models, upon charging, desodiation initiates near the separator and proceeds faster in the region between the separator and the fiber. This leads to strong SoS heterogeneities, up to 20%, between the separator side and the current collector side of the electrode (Fig. 6c and Fig. S10, S11). During discharge, the desodiation front starts near the separator and gradually propagates deeper into the electrode, result-

Open Access Article. Published on 13 February 2026. Downloaded on 2/25/2026 4:41:42 AM.
This article is licensed under a Creative Commons Attribution-NonCommercial 3.0 Unported Licence.

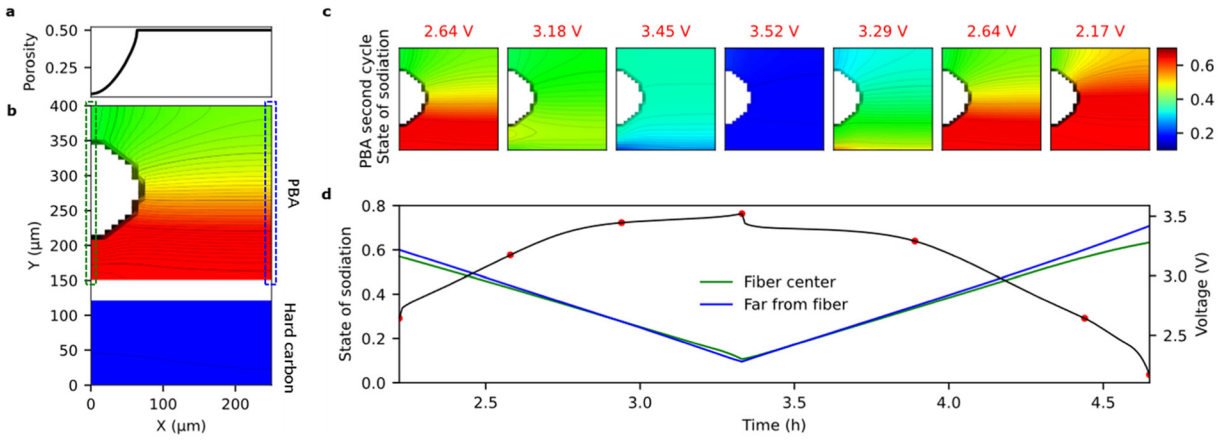

Fig. 6 (a) In-plane porosity profile of the PBA positive electrode. (b) Schematic of the simulated cell configuration, consisting (from bottom to top) of the hard carbon negative electrode, separator, and PBA positive electrode. The inactive white semi-circular region represents the embedded optical fiber. Dashed frames highlight the regions at the fiber center and far from the fiber. (c) Evolution of the sodium concentration distribution in the PBA positive electrode during the second cycle at a 0.5 C rate. (d) State of sodiation (SoS) profiles in the two regions, plotted alongside the cell's OCV curve. Red dots correspond to the voltages of the snapshots shown in (c).

ing in similar SoS heterogeneities. At first glance, no apparent differences in the SoS exist between the fiber center and regions far from the fiber. Turning to a more quantitative analysis, the SoS evolution during cycling far and close to the fiber are extracted (Fig. 6d). For both models, SoS evolution far and close from the fiber does not overlap, showing that indeed the fiber influences the reactivity. For model 1, the simulated local C-rate at the fiber position is higher than that far from the fiber. This is not in agreement with the experimental observations; hence, model 1 is ruled out (Fig. S10). In contrast, the local C-rate evolution for model 2 shows a systematically lower value close to the fiber position, qualitatively reproducing our observations.

These preliminary simulations are encouraging and suggest that the reduction of the porosity due to the compression of the electrode at the fiber position might be one of the possible origins of the delay. Other mechanisms could explain the delay such as wetting issues close to the fiber or the heterogeneous current density at the fiber position. Note that our simulations also show that the reaction is heterogeneous in the depth of the electrode, and hence the SoS measured from a fiber will depend on its depth in the electrode. A large experimental campaign guided by modelling could be a future direction to precisely understand how to tackle this electrochemical lag.

Conclusion

This study comprehensively evaluates optical fiber sensors for state-of-charge (SoC) monitoring in Na-ion batteries, combining *operando* infrared spectroscopy with spatially resolved synchrotron X-ray scattering techniques. By implementing a TAS optical fiber within a hard carbon/Prussian blue analog pouch cell, we investigated both the capabilities and limitations of fiber-based SoC sensing. The *operando* IR-OFEWS measurements successfully captured qualitative changes in the state-of-sodiation of PBA positive electrodes through characteristic C≡N vibration modes at 2055 cm^{-1} (R-PW) and 2178 cm^{-1} (T-PY). However, spatially resolved μWAXS/SAXS mapping revealed two critical limitations: (1) substantial electrode-level heterogeneity across length scales from 100 μm to several millimeters, which cannot be captured by a single fiber as it only detects a micrometric cylinder along the entire length of the electrode, whereas the electrode is several cm wide, and (2) localized perturbations at the fiber position resulting in consistently higher SoS values (5–20% delay for the cell studied in this work) compared to surrounding regions. Preliminary pseudo-3D modelling suggests that the electrochemical delay at the fiber position could originate from compression-induced changes in the electrode microstructure that locally hinder charge-discharge kinetics. This work highlights the challenges and opportunities of using optical fibers for *operando* SoC sensing, advancing our understanding of localized interactions and providing a foundation for the development of accurate and minimally invasive sensing technologies.

Author contributions

Y.-C. Y. and Y. W. equally contributed to this work. Q. J., S. L., and J.-M. T. designed the study. Y. W., N. M. K., Z. L., O. S., and J.-M. T. prepared the materials, cells, performed the SEM, the *operando* IR and the electrochemical measurements. Y.-C. Y., Y. W., A. O., S. L., A. V. R., Q. J., and S. T. participated in the SAXS/WAXS experiment, N. B. prepared and aligned the BM02 beamline, Y.-C. Y., A. O., S. L., and Q. J. analyzed the SAXS/WAXS data. A. V. R. and B. M. performed the simulation. Y.-C. Y., Y. W., A. O., A. V. R., and Q. J. wrote the manuscript; all authors participated in the final edition and discussions.

 © 2026 The Author(s). Published by the Royal Society of Chemistry

Open Access Article. Published on 13 February 2026. Downloaded on 2/25/2026 4:41:42 AM.
This article is licensed under a Creative Commons Attribution-NonCommercial 3.0 Unported Licence.

Conflicts of interest

There are no conflicts to declare.

Data availability

The raw data are accessible at European Synchrotron Radiation Facility at https://doi.org/10.15151/ESRF-DC-2262510184. Data analysis was performed with a homemade python code which can be shared on request. Inkscape was used for making figures (https://inkscape.org/).

Supplementary information (SI) is available. See DOI: https://doi.org/10.1039/d6eb00019c.

Acknowledgements

The beamtime at the ESRF was granted within the Battery Pilot Hub MA4929 "Multi-scale Multi-techniques investigations of Li-ion batteries: towards a European Battery Hub". Yu Wang is thankful to the SensOLib - projet ANR-22-CE05-0031-01 for funding.

References

1 M. Berecibar, I. Gandiaga, I. Villarreal, N. Omar, J. Van Mierlo and P. Van den Bossche, Critical Review of State of Health Estimation Methods of Li-Ion Batteries for Real Applications, *Renewable Sustainable Energy Rev.*, 2016, **56**, 572–587, DOI: 10.1016/j.rser.2015.11.042.

2 Y. Che, X. Hu, X. Lin, J. Guo and R. Teodorescu, Health Prognostics for Lithium-Ion Batteries: Mechanisms, Methods, and Prospects, *Energy Environ. Sci.*, 2023, **16**(2), 338–371, DOI: 10.1039/D2EE03019E.

3 J. Amici, P. Asinari, E. Ayerbe, P. Barboux, P. Bayle-Guillemaud, R. J. Behm, M. Berecibar, E. Berg, A. Bhowmik, S. Bodoardo, I. E. Castelli, I. Cekic-Laskovic, R. Christensen, S. Clark, R. Diehm, R. Dominko, M. Fichtner, A. A. Franco, A. Grimaud, N. Guillet, M. Hahlin, S. Hartmann, V. Heiries, K. Hermansson, A. Heuer, S. Jana, L. Jabbour, J. Kallo, A. Latz, H. Lorrmann, O. M. Løvvik, S. Lyonnard, M. Meeus, E. Paillard, S. Perraud, T. Placke, C. Punckt, O. Raccurt, J. Ruhland, E. Sheridan, H. Stein, J.-M. Tarascon, V. Trapp, T. Vegge, M. Weil, W. Wenzel, M. Winter, A. Wolf and K. Edström, A Roadmap for Transforming Research to Invent the Batteries of the Future Designed within the European Large Scale Research Initiative BATTERY 2030+, *Adv. Energy Mater.*, 2022, **12**(17), 2102785, DOI: 10.1002/aenm.202102785.

4 R. Xiong, L. Li and J. Tian, Towards a Smarter Battery Management System: A Critical Review on Battery State of Health Monitoring Methods, *J. Power Sources*, 2018, **405**, 18–29, DOI: 10.1016/j.jpowsour.2018.10.019.

5 M. R. Palacín, Understanding, Ageing in Li-Ion Batteries: A Chemical Issue, *Chem. Soc. Rev.*, 2018, **47**(13), 4924–4933, DOI: 10.1039/C7CS00889A.

6 S. Novais, M. Nascimento, L. Grande, M. F. Domingues, P. Antunes, N. Alberto, C. Leitão, R. Oliveira, S. Koch, G. T. Kim, S. Passerini and J. Pinto, Internal and External Temperature Monitoring of a Li-Ion Battery with Fiber Bragg Grating Sensors, *Sensors*, 2016, **16**(9), 1394, DOI: 10.3390/s16091394.

7 L. Albero Blanquer, F. Marchini, J. R. Seitz, N. Daher, F. Bétermier, J. Huang, C. Gervillié and J.-M. Tarascon, Optical Sensors for Operando Stress Monitoring in Lithium-Based Batteries Containing Solid-State or Liquid Electrolytes, *Nat. Commun.*, 2022, **13**(1), 1153, DOI: 10.1038/s41467-022-28792-w.

8 L. W. Sommer, A. Raghavan, P. Kiesel, B. Saha, J. Schwartz, A. Lochbaum, A. Ganguli, C.-J. Bae and M. Alamgir, Monitoring of Intercalation Stages in Lithium-Ion Cells over Charge-Discharge Cycles with Fiber Optic Sensors, *J. Electrochem. Soc.*, 2015, **162**(14), A2664, DOI: 10.1149/2.0361514jes.

9 A. Ghannoum, R. C. Norris, K. Iyer, L. Zdravkova, A. Yu and P. Nieva, Optical Characterization of Commercial Lithiated Graphite Battery Electrodes and in Situ Fiber Optic Evanescent Wave Spectroscopy, *ACS Appl. Mater. Interfaces*, 2016, **8**(29), 18763–18769, DOI: 10.1021/acsami.6b03638.

10 C. Gervillié-Mouravieff, W. Bao, D. A. Steingart and Y. S. Meng, Non-Destructive Characterization Techniques for Battery Performance and Life-Cycle Assessment, *Nat. Rev. Electr. Eng.*, 2024, **1**(8), 547–558, DOI: 10.1038/s44287-024-00069-y.

11 A. Olgo, S. Genies, R. Franchi, C. Septet, Q. Jacquet, Q. Berrod, R. Palm, P. Chenevier, E. Villemin, C. Villevieille, N. Blanc, S. Tardif, O. Raccurt and S. Lyonnard, Revealing How Internal Sensors in a Smart Battery Impact the Local Graphite Lithiation Mechanism, *Nat. Commun.*, 2024, **15**(1), 10258, DOI: 10.1038/s41467-024-54656-6.

12 C. Gervillié-Mouravieff, C. Boussard-Plédel, J. Huang, C. Leau, L. A. Blanquer, M. B. Yahia, M. L. Doublet, S. T. Boles, X. H. Zhang, J. L. Adam and J. M. Tarascon, Unlocking Cell Chemistry Evolution with Operando Fibre Optic Infrared Spectroscopy in Commercial Na(Li)-Ion Batteries, *Nat. Energy*, 2022, **7**(12), 1157–1169, DOI: 10.1038/s41560-022-01141-3.

13 J. Huang, C. Delacourt, P. Desai and J.-M. Tarascon, Operando Entropy Profiling of Sodium-Ion Batteries via Optical Fiber Sensing for Thermal Management and Ageing Monitoring, *J. Electrochem. Soc.*, 2024, **171**(3), 030516, DOI: 10.1149/1945-7111/ad30da.

14 R. Wang, H. Zhang, Q. Liu, F. Liu, X. Han, X. Liu, K. Li, G. Xiao, J. Albert, X. Lu and T. Guo, Operando Monitoring of Ion Activities in Aqueous Batteries with Plasmonic Fiber-Optic Sensors, *Nat. Commun.*, 2022, **13**(1), 547, DOI: 10.1038/s41467-022-28267-y.

Open Access Article. Published on 13 February 2026. Downloaded on 2/25/2026 4:41:42 AM.
This article is licensed under a Creative Commons Attribution-NonCommercial 3.0 Unported Licence.

15 Z. Li, Y. Wang, F. Rabuel, M. Deschamps, G. Rousse, O. Sel and J.-M. Tarascon, Na2-*x*Mn[Fe(CN)6] Prussian Blue Analog Cathodes for Na-Ion Batteries – From Fundamentals to Practical Demonstration, *Energy Storage Mater.*, 2025, **76**, 104118, DOI: 10.1016/j.ensm.2025.104118.

16 K. Hurlbutt, S. Wheeler, I. Capone and M. Pasta, Prussian Blue Analogs as Battery Materials, *Joule*, 2018, **2**(10), 1950–1960, DOI: 10.1016/j.joule.2018.07.017.

17 J. Song, L. Wang, Y. Lu, J. Liu, B. Guo, P. Xiao, J. J. Lee, X. Q. Yang, G. Henkelman and J. B. Goodenough, Removal of Interstitial H_2O in Hexacyanometallates for a Superior Cathode of a Sodium-Ion Battery, *J. Am. Chem. Soc.*, 2015, **137**(7), 2658–2664, DOI: 10.1021/JA512383B/SUPPL_FILE/JA512383B_SI_002.CIF.

18 J. M. Tarascon, A. S. Gozdz, C. Schmutz, F. Shokoohi and P. C. Warren, Performance of Bellcore's Plastic Rechargeable Li-Ion Batteries, *Solid State Ionics*, 1996, **86–88**, 49–54, DOI: 10.1016/0167-2738(96)00330-X.

19 T. Jousseaume, J.-F. Colin, M. Chandesris, S. Lyonnard and S. Tardif, How Beam Damage Can Skew Synchrotron Operando Studies of Batteries, *ACS Energy Lett.*, 2023, **8**(8), 3323–3329, DOI: 10.1021/acsenergylett.3c00815.

20 A. P. Black, C. Escudero, F. Fauth, M. Fehse, G. Agostini, M. Reynaud, R. G. Houdeville, D. Chatzogiannakis, J. Orive, A. Ramo-Irurre, M. Casas-Cabanas and M. R. Palacin, Beam Effects in Synchrotron Radiation Operando Characterization of Battery Materials: X-Ray Diffraction and Absorption Study of LiNi0.33Mn0.33Co0.33O2 and LiFePO4 Electrodes, *Chem. Mater.*, 2024, **36**(11), 5596–5610, DOI: 10.1021/acs.chemmater.4c00597.

21 J. Kieffer and D. Karkoulis, PyFAI, a Versatile Library for Azimuthal Regrouping, *J. Phys.: Conf. Ser.*, 2013, **425**(20), 202012, DOI: 10.1088/1742-6596/425/20/202012.

22 E. Flores, M. Mozhzhukhina, X. Li, P. Norby, A. Matic and T. Vegge, PRISMA: A Robust and Intuitive Tool for High-Throughput Processing of Chemical Spectra, *Chem. Methods*, 2022, **2**(10), e202100094, DOI: 10.1002/cmtd.202100094.

23 C. Matei Ghimbeu, A. Beda, B. Réty, H. El Marouazi, A. Vizintin, B. Tratnik, L. Simonin, J. Michel, J. Abou-Rjeily and R. Dominko, Review: Insights on Hard Carbon Materials for Sodium-Ion Batteries (SIBs): Synthesis – Properties – Performance Relationships, *Adv. Energy Mater.*, 2024, **14**(19), 2303833, DOI: 10.1002/aenm.202303833.

24 *Revealing the Sodium Storage Mechanisms in Hard Carbon Pores - Kitsu Iglesias - 2023 - Advanced Energy Materials - Wiley Online Library*. https://onlinelibrary.wiley.com/doi/full/10.1002/aenm.202302171 (accessed 2025–02–14).

25 G. Oney, F. Monaco, S. Mitra, A. Medjahed, M. Burghammer, D. Karpov, M. Mirolo, J. Drnec, I. C. Jolivet, Q. Arnoux, S. Tardif, Q. Jacquet and S. Lyonnard, Slow, and Overworked Graphite: Operando X-Ray Microdiffraction Mapping of Aged Electrodes, *Adv. Energy Mater.*, 2025, **15**, e02032.

26 E. Lübke, L. Helfen, P. Cook, M. Mirolo, V. Vinci, O. Korjus, B. Fuchsbichler, S. Koller, R. Brunner, J. Drnec and S. Lyonnard, The Origins of Critical Deformations in Cylindrical Silicon Based Li-Ion Batteries, *Energy Environ. Sci.*, 2024, **17**(14), 5048–5059, DOI: 10.1039/D4EE00590B.

27 M. Klett, R. Eriksson, J. Groot, P. Svens, K. Ciosek Högström, R. W. Lindström, H. Berg, T. Gustafson, G. Lindbergh and K. Edström, Non-Uniform Aging of Cycled Commercial LiFePO4//Graphite Cylindrical Cells Revealed by *Post-Mortem* Analysis, *J. Power Sources*, 2014, **257**, 126–137, DOI: 10.1016/j.jpowsour.2014.01.105.

28 A. Franco, Multiscale Modelling and, Numerical Simulation of Rechargeable Lithium Ion Batteries: Concepts, Methods and Challenges, *RSC Adv.*, 2013, **3**(32), 13027–13058, DOI: 10.1039/C3RA23502E.

29 M. Doyle, T. F. Fuller and J. Newman, Modeling of Galvanostatic Charge and Discharge of the Lithium/Polymer/Insertion Cell, *J. Electrochem. Soc.*, 1993, **140**(6), 1526, DOI: 10.1149/1.2221597.

30 Q. Jacquet, I. Profatilova, L. Baggetto, B. Alrifai, E. Addes, P. Chassagne, N. Blanc, S. Tardif, L. Daniel and S. Lyonnard, Mapping Reaction Mechanism During Overcharge of a LiNiO2/Graphite–Silicon Lithium-Ion Battery: A Correlative Operando Approach by Simultaneous Gas Analysis and Synchrotron Scattering Techniques, *Adv. Energy Mater.*, 2025, 2404080, DOI: 10.1002/aenm.202404080.

31 C. L. Berhaut, M. Mirolo, D. Z. Dominguez, I. Martens, S. Pouget, N. Herlin-Boime, M. Chandesris, S. Tardif, J. Drnec and S. Lyonnard, Charge Dynamics Induced by Lithiation Heterogeneity in Silicon-Graphite Composite Anodes, *Adv. Energy Mater.*, 2023, **13**(44), 2301874, DOI: 10.1002/aenm.202301874.

32 D. Petz, M. J. Mühlbauer, V. Baran, A. Schökel, V. Kochetov, M. Hofmann, V. Dyadkin, P. Staron, G. Vaughan, U. Lienert, P. Müller-Buschbaum and A. Senyshyn, Lithium Distribution and Transfer in High-Power 18650-Type Li-Ion Cells at Multiple Length Scales, *Energy Storage Mater.*, 2021, **41**, 546–553, DOI: 10.1016/j.ensm.2021.06.028.

33 T. M. M. Heenan, I. Mombrini, A. Llewellyn, S. Checchia, C. Tan, M. J. Johnson, A. Jnawali, G. Garbarino, R. Jervis, D. J. L. Brett, M. Di Michiel and P. R. Shearing, Mapping Internal Temperatures during High-Rate Battery Applications, *Nature*, 2023, **617**(7961), 507–512, DOI: 10.1038/s41586-023-05913-z.

34 S. Tardif, N. Dufour, J.-F. Colin, G. Gébel, M. Burghammer, A. Johannes, S. Lyonnard and M. Chandesris, Combining Operando X-Ray Experiments and Modelling to Understand the Heterogeneous Lithiation of Graphite Electrodes, *J. Mater. Chem. A*, 2021, **9**(7), 4281–4290, DOI: 10.1039/D0TA10735B.

35 J. Huang, L. A. Blanquer, C. Gervillié and J.-M. Tarascon, Distributed Fiber Optic Sensing to Assess In-Live Temperature Imaging Inside Batteries: Rayleigh and FBGs, *J. Electrochem. Soc.*, 2021, **168**(6), 060520, DOI: 10.1149/1945-7111/ac03f0.

36 K. Li, Y. Huang, G. Han, W. Lyu, A. He, N. Liu, Y. Yu and Y. Huang, Real-Time Electrochemical-Strain Distribution and State-of-Charge Mapping via Distributed Optical Fiber for Lithium-Ion Batteries, *J. Power Sources*, 2024, **624**, 235526, DOI: 10.1016/j.jpowsour.2024.235526.

 © 2026 The Author(s). Published by the Royal Society of Chemistry